Published OnlineFirst September 30, 2013; DOI: 10.1158/1078-0432.CCR-13-0742

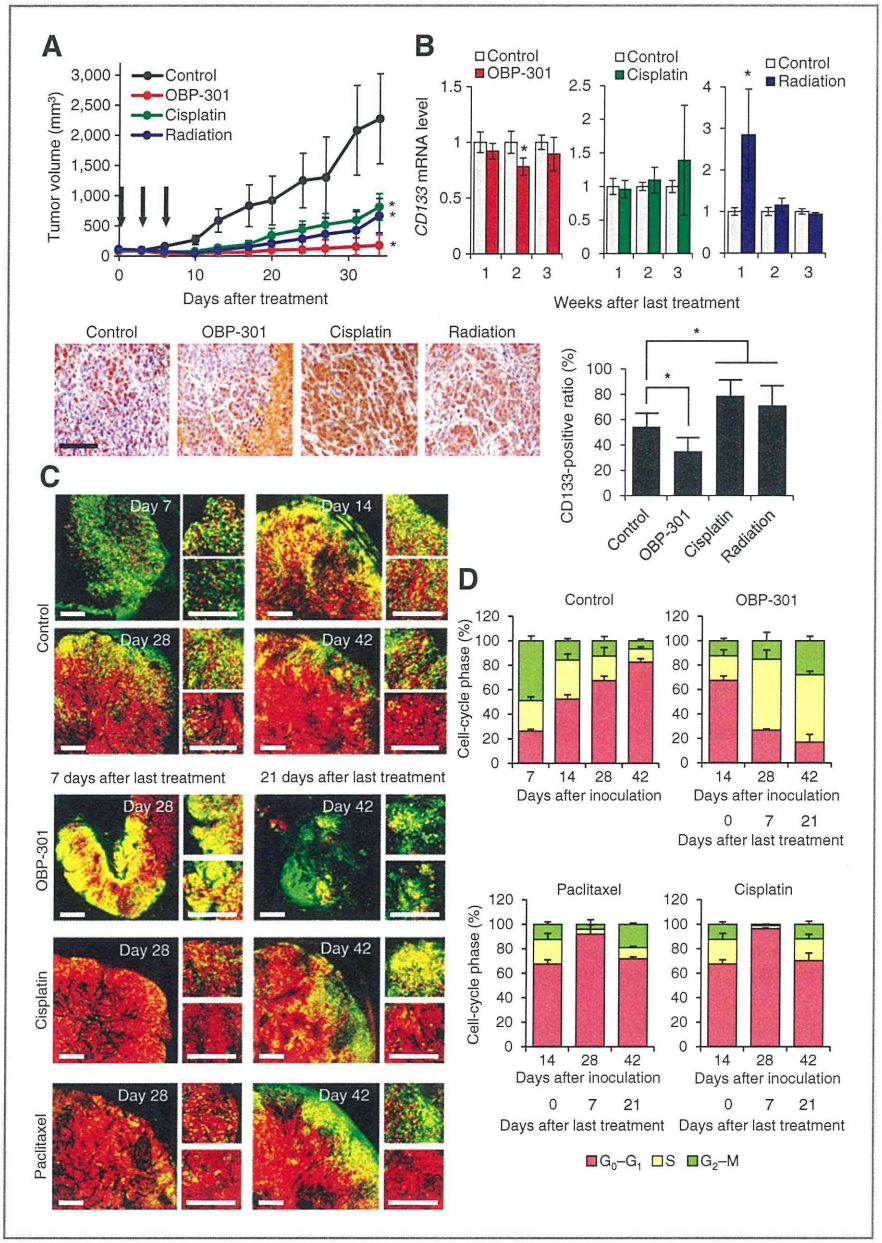

Figure 5. OBP-301 induces cell-cycle progression and efficiently kills dormant cancer cells resistant to conventional therapy in established human tumor xenografts. $CD133^+$-rich radioresistant MKN45 cells (5×10^6 cells/mouse) were injected subcutaneously into the left flanks of mice. When the tumors reached approximately 6 mm in diameter (tumor volume, 100–120 mm^3), mice were administered OBP-301 intratumorally (1×10^8 PFU/tumor), injected intraperitoneally with cisplatin (4 mg/kg), or exposed to 2 Gy of radiation for 3 cycles every 3 days. A, growth curves of tumors derived from radioresistant MKN45 cells after treatment with OBP-301, cisplatin or radiation. Black arrows indicate the day of treatment. B, expression of *CD133* mRNA in tumors treated with OBP-301, cisplatin, or radiation at 1, 2, and 3 weeks after treatment (top). Representative images of CD133-stained tumor section treated with OBP-301, cisplatin, or radiation (bottom left). Scale bars, 100 μm. Histogram shows the percentages of $CD133^+$ cells in tumors treated with OBP-301, cisplatin, or radiation (bottom right). The percentage of $CD133^+$ cells was calculated by dividing the number of $CD133^+$ cells by the total number of cells. Data are shown as means ± SD ($n = 3$). *, $P < 0.05$. C and D, FUCCI-expressing MKN45 cells (5×10^6 cells/mouse) were injected subcutaneously into the left flanks of mice. When the tumors reached approximately 7 mm in diameter (tumor volume, 150–180 mm^3), mice were administered OBP-301 intratumorally (1×10^8 PFU/tumor), injected intraperitoneally with cisplatin (4 mg/kg) or paclitaxel (5 mg/kg) for 3 cycles every 3 days. Representative images of cross-sections of FUCCI-expressing MKN45 subcutaneous tumors of control, OBP-301-, cisplatin-, or paclitaxel-treated mice (left). The cells in G_0–G_1, S, or G_2–M phases appear red, yellow, or green, respectively. Histogram shows the cell-cycle phase of FUCCI-expressing MKN45 subcutaneous tumor from control, OBP-301-, cisplatin-, or paclitaxel-treated mice (right). The percentage of cells in G_0–G_1, S, and G_2–M phases are shown. Data are shown as means ± SD ($n = 5$). *, $P < 0.05$. Scale bars, 500 μm.

Published OnlineFirst September 30, 2013; DOI: 10.1158/1078-0432.CCR-13-0742

After cisplatin or paclitaxel treatment, the tumor consisted mostly of red fluorescent cells (Fig. 5D), indicating that the cytotoxic agents killed only cycling cancer cells and had little effect on quiescent dormant cancer cells. These tumors regrew, with the quiescent cells re-entering the cell cycle 21 days after last treatment (Fig. 5D). In contrast, intratumor injection of OBP-301 mobilized the cancer cells into the S/G_2/M phase trap, leading to elimination of cancer cells in S/G_2/M phases (Fig. 5D). These data indicate that OBP-301 could efficiently kill quiescent cancer stem–like cells in tumors by inducing cell-cycle progression.

OBP-301 sensitizes quiescent cancer stem–like cells to chemotherapy by cell-cycle mobilization and S/G_2/M phase trapping

As we previously showed that OBP-301 enhances the sensitivities to chemotherapeutic agents in various types of human cancer cells (30, 31), we further evaluated whether OBP-301 sensitizes quiescent CD133$^+$ cancer stem–like cells to chemotherapy by inducing cell-cycle progression and S/G_2/M phase trapping. OBP-301 infection significantly enhanced the inhibitory effect of chemotherapy on cell viability and tumor sphere formation of CD133$^+$ cells (Fig. 6A and Supplementary

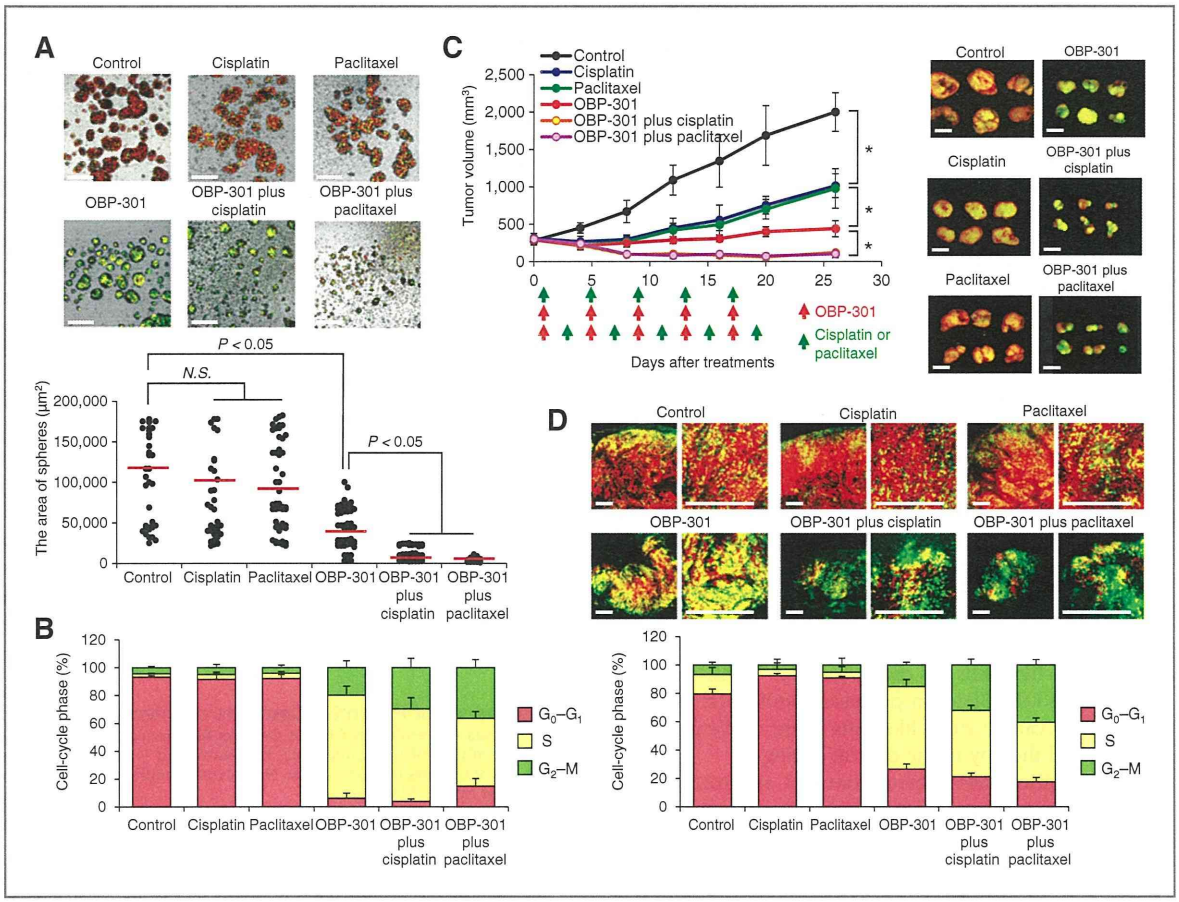

Figure 6. OBP-301 sensitizes quiescent CD133$^+$ cancer stem–like cells to chemotherapy by inducing cell-cycle progression. A, representative images of tumor spheres from FUCCI-expressing CD133$^+$ cells after treatment with cisplatin, paclitaxel, OBP-301, and the combination of OBP-301 and chemotherapy (top). The cells in G_0–G_1, S, or G_2–M phases appear red, yellow, or green, respectively. The tumor-sphere area was calculated using NIH ImageJ software (lower). Data are shown as means ± SD ($n = 5$). *, $P < 0.05$. Scale bars, 500 μm. B, histogram shows the cell-cycle phase of tumor spheres from FUCCI-expressing CD133$^+$ cells after treatment with chemotherapy, OBP-301, and the combination of OBP-301 and chemotherapy. The percentage of cells in G_0–G_1, S, and G_2–M phases are shown. Data are shown as means ± SD ($n = 5$). *, $P < 0.05$. C, FUCCI-expressing MKN45 cells (5×10^6 cells/mouse) were injected subcutaneously into the left flanks of mice. When the tumors reached approximately 8 mm in diameter (tumor volume, 300 mm^3), mice were administered OBP-301 intratumorally (1×10^8 PFU/tumor), injected intraperitoneally with cisplatin (4 mg/kg) or paclitaxel (5 mg/kg) for 5 cycles every 3 days. The growth curves of tumors derived from FUCCI-expressing MKN45 cells after treatment with chemotherapy, OBP-301, or the combination of OBP-301 and chemotherapy (left). Red and green arrows indicate the day of treatment with OBP-301 and chemotherapy, respectively. Macroscopic photographs of FUCCI-expressing tumors in untreated (control) or treated with OBP-301, cisplatin, paclitaxel, or the combination of OBP-301 and chemotherapy (right). Scale bars, 10 mm. D, representative image of cross-sections of FUCCI-expressing MKN45 subcutaneous tumors of control, OBP-301-, cisplatin-, paclitaxel-, or the combination of OBP-301- and chemotherapy-treated mice (top). Histogram shows cell-cycle phase of FUCCI-expressing MKN45 subcutaneous tumors of control, treated with OBP-301, cisplatin, paclitaxel, or the combination of OBP-301 and chemotherapy (bottom). Data are shown as means ± SD ($n = 6$). *, $P < 0.05$, ANOVA. Scale bars, 500 μm.

Published OnlineFirst September 30, 2013; DOI: 10.1158/1078-0432.CCR-13-0742

Fig. S13). Tumor spheres treated with chemotherapy and OBP-301 contained an increased percentage of tumor cells in G_2–M phases compared to OBP-301 alone (Fig. 6B). The combination of OBP-301 and chemotherapy (Supplementary Fig. S10C) significantly suppressed tumor growth compared to chemotherapy or OBP-301 alone (Fig. 6C and Supplementary Fig. S14). Cross-sections of tumor tissues showed that the combination of chemotherapy and OBP-301 induced an increased percentage of cancer cells in G_2–M phases compared to OBP-301 alone (Fig. 6D). These results suggest that OBP-301 sensitizes the quiescent cancer stem–like cells to chemotherapy-mediated G_2–M arrest by inducing cell-cycle progression and S/G_2/M phase trapping.

Discussion

We have described that a bioengineered telomerase-specific oncolytic adenovirus, OBP-301, efficiently kills $CD133^+$ cancer stem–like cells that have elevated telomerase activity through enhanced E1A-mediated cell-cycle mobilization and S-phase trapping. By using FUCCI technology in combination with tumor sphere culture, we visualized virus penetration, cell-cycle dynamics, and the subsequent elimination of quiescent cancer stem–like cells in dormant tumor spheres (Supplementary Fig. S15A).

Cancer stem–like cells have been shown to be highly resistant to chemotherapeutic agents (32, 33) and ionizing radiation (24–26). As expected, $CD133^+$ human gastric cancer cells were more resistant to conventional therapies than $CD133^-$ cells; OBP-301, however, efficiently reduced the viability of $CD133^+$ cells, similar to their reduction of viability of $CD133^-$ cells. Moreover, we showed that OBP-301 significantly reduced the stem cell properties of $CD133^+$ cells *in vitro* and *in vivo* compared with conventional chemoradiotherapy and further sensitized $CD133^+$ cancer stem–like cells to chemotherapy. These findings indicate that OBP-301 is a promising anticancer therapy to eliminate cancer stem–like cells more efficiently than conventional therapy in the clinical setting.

Recent studies have showed that p53 and $p21^{cip1/waf1}$ maintain the quiescent state in hematopoietic stem cells (34, 35). Moreover, $p27^{kip1}$ has been suggested to be involved in suppression of the transition from the G_0 phase to G_1–S phases (36, 37). Cancer stem–like cells maintain a more quiescent state than non–cancer stem–like cells, which is associated with cancer stem–like cell resistance to conventional therapies (9, 10). OBP-301 induced S and G_2–M phase entry and subsequent cell death in quiescent $CD133^+$ cells through upregulation of E2F1-related proteins and downregulation of p53-related and p27 proteins in an E1A-dependent manner. A recent report suggested that suppression of the p53-mediated G_1 checkpoint is required for E2F1-induced S-phase entry (38). Furthermore, adenoviral E1A has been shown to suppress p53-mediated cell-cycle arrest after DNA damage (39). Thus, OBP-301 can inhibit cancer stem–like cells from maintaining a quiescent state and force them into cycling by not only upregulating E2F-related proteins but also downregulating p53-related and p27 proteins (Supplementary Fig. S15B), leading to the sensitization to chemotherapy.

FUCCI (23) is a powerful tool to visualize the quiescent state in cancer stem–like cells and the treatment dynamics of OBP-301. When tumor spheres were formed, $CD133^+$ cells maintained a quiescent state, which was defined by red fluorescent nuclei expressed in G_0–G_1 phases. In contrast, S and G_2–M phase entry induced by OBP-301 could be clearly visualized as yellow and green fluorescent nuclei, respectively. Our data indicate that 3-dimensional cultures are extremely important for the maintenance of the quiescence of $CD133^+$ cells. FUCCI-based real-time imaging of the cell cycle provides a platform for the screening of candidate therapeutic agents that modulate the quiescent state of drug-resistant cancer stem–like cells.

In conclusion, we have clearly shown that a genetically-engineered oncolytic adenovirus, OBP-301, efficiently eradicates quiescent cancer stem–like cells in solid tumors by cell-cycle mobilization and S/G_2/M phase trapping. A phase I clinical trial of intratumoral injection of OBP-301 in patients with advanced solid tumors was recently completed and OBP-301 monotherapy was well tolerated by these patients (20). However, the difficulty of adenoviral delivery to inaccessible primary and metastatic tumor tissues is a major obstacle for clinical translation of this treatment modality. In this study, the combination therapy of OBP-301 with chemotherapy was highly effective antitumor therapy to eliminate both cancer stem–like and non–cancer stem–like cells in a xenograft model. Future clinical trials of intratumoral injection of OBP-301 in combination with conventional antitumor therapy are suggested by the results of the present study.

Disclosure of Potential Conflicts of Interest

Y. Urata is President & CEO of Oncolys BioPharma, Inc., the manufacturer of OBP-301 (Telomelysin). H. Tazawa and T. Fujiwara are consultants of Oncolys BioPharma, Inc. No potential conflicts of interest were disclosed by the other authors.

Authors' Contributions

Conception and design: S. Yano, H. Tazawa, R. M. Hoffman, T. Fujiwara
Development of methodology: S. Yano, H. Tazawa, Y. Hashimoto, S. Kuroda, H. Kishimoto
Acquisition of data (provided animals, provided facilities, etc): S. Yano, H. Tazawa, Y. Hashimoto
Analysis and interpretation of data (e.g., statistical analysis, biostatistics, computational analysis): S. Yano, H. Tazawa, Y. Hashimoto, Nagasaka, S. Kagawa, T. Fujiwara
Writing, review, and/or revision of manuscript: S. Yano, H. Tazawa, R. M. Hoffman, T. Fujiwara
Administrative, technical, or material support: Y. Urata, R. M. Hoffman
Study supervision: H. Tazawa, Y. Shirakawa, M. Nishizaki, T. Nagasaka, S. Kagawa, R. M. Hoffman, T. Fujiwara

Acknowledgments

The authors thank Yukinari Isomoto and Tomoko Sueishi for their technical support.

Published OnlineFirst September 30, 2013; DOI: 10.1158/1078-0432.CCR-13-0742

Grant Support

This work was supported, in part, by grants from the Ministry of Education, Culture, Sports, Science, and Technology of Japan (to T. Fujiwara, No. 22390256) and by grants from the Ministry of Health, Labour, and Welfare of Japan (to T. Fujiwara, No. 10103827, No. 09156285).

The costs of publication of this article were defrayed in part by the payment of page charges. This article must therefore be hereby marked *advertisement* in accordance with 18 U.S.C. Section 1734 solely to indicate this fact.

Received March 20, 2013; revised September 10, 2013; accepted September 10, 2013; published OnlineFirst September 30, 2013.

References

1. Goss PE, Chambers AF. Does tumour dormancy offer a therapeutic target? Nat Rev Cancer 2010;10:871–7.
2. Aguirre-Ghiso JA. Models, mechanisms and clinical evidence for cancer dormancy. Nat Rev Cancer 2007;7:834–46.
3. Reya T, Morrison SJ, Clarke MF, Weissman IL. Stem cells, cancer, and cancer stem cells. Nature 2001;414:105–11.
4. Pardal R, Clarke MF, Morrison SJ. Applying the principles of stem-cell biology to cancer. Nat Rev Cancer 2003;3:895–902.
5. Clarke MF, Dick JE, Dirks PB, Eaves CJ, Jamieson CH, Jones DL, et al. Cancer stem cells–perspectives on current status and future directions: AACR Workshop on cancer stem cells. Cancer Res 2006;66:9339–44.
6. Visvader JE, Lindeman GJ. Cancer stem cells in solid tumours: accumulating evidence and unresolved questions. Nat Rev Cancer 2008;8:755–68.
7. Trumpp A, Wiestler OD. Mechanisms of Disease: cancer stem cells–targeting the evil twin. Nat Clin Pract Oncol 2008;5:337–47.
8. Zhou BB, Zhang H, Damelin M, Geles KG, Grindley JC, Dirks PB. Tumour-initiating cells: challenges and opportunities for anticancer drug discovery. Nat Rev Drug Discov 2009;8:806–23.
9. Ito K, Bernardi R, Morotti A, Matsuoka S, Saglio G, Ikeda Y, et al. PML targeting eradicates quiescent leukaemia-initiating cells. Nature 2008;453:1072–8.
10. Saito Y, Uchida N, Tanaka S, Suzuki N, Tomizawa-Murasawa M, Sone A, et al. Induction of cell cycle entry eliminates human leukemia stem cells in a mouse model of AML. Nat Biotechnol 2010;28:275–80.
11. Alemany R, Balague C, Curiel DT. Replicative adenoviruses for cancer therapy. Nat Biotechnol 2000;18:723–7.
12. Russell SJ, Peng KW, Bell JC. Oncolytic virotherapy. Nat Biotechnol 2012;30:658–70.
13. Stracker TH, Carson CT, Weitzman MD. Adenovirus oncoproteins inactivate the Mre11-Rad50-NBS1 DNA repair complex. Nature 2002;418:348–52.
14. Flinterman M, Gaken J, Farzaneh F, Tavassoli M. E1A-mediated suppression of EGFR expression and induction of apoptosis in head and neck squamous carcinoma cell lines. Oncogene 2003;22:1965–77.
15. Yu D, Wolf JK, Scanlon M, Price JE, Hung MC. Enhanced c-erbB-2/neu expression in human ovarian cancer cells correlates with more severe malignancy that can be suppressed by E1A. Cancer Res 1993;53:891–8.
16. Eriksson M, Guse K, Bauerschmitz G, Virkkunen P, Tarkkanen M, Tanner M, et al. Oncolytic adenoviruses kill breast cancer initiating CD44+CD24-/low cells. Mol Ther 2007;15:2088–93.
17. Zhang X, Komaki R, Wang L, Fang B, Chang JY. Treatment of radioresistant stem-like esophageal cancer cells by an apoptotic gene-armed, telomerase-specific oncolytic adenovirus. Clin Cancer Res 2008;14:2813–23.
18. Kanai R, Rabkin SD, Yip S, Sgubin D, Zaupa CM, Hirose Y, et al. Oncolytic virus-mediated manipulation of DNA damage responses: synergy with chemotherapy in killing glioblastoma stem cells. J Natl Cancer Inst 2012;104:42–55.
19. Kawashima T, Kagawa S, Kobayashi N, Shirakiya Y, Umeoka T, Teraishi F, et al. Telomerase-specific replication-selective virotherapy for human cancer. Clin Cancer Res 2004;10:285–92.
20. Nemunaitis J, Tong AW, Nemunaitis M, Senzer N, Phadke AP, Bedell C, et al. A phase I study of telomerase-specific replication competent oncolytic adenovirus (telomelysin) for various solid tumors. Mol Ther 2010;18:429–34.
21. Yokozaki H. Molecular characteristics of eight gastric cancer cell lines established in Japan. Pathol Int 2000;50:767–77.
22. Hashimoto Y, Watanabe Y, Shirakiya Y, Uno F, Kagawa S, Kawamura H, et al. Establishment of biological and pharmacokinetic assays of telomerase-specific replication-selective adenovirus. Cancer Sci 2008;99:385–90.
23. Sakaue-Sawano A, Kurokawa H, Morimura T, Hanyu A, Hama H, Osawa H, et al. Visualizing spatiotemporal dynamics of multicellular cell-cycle progression. Cell 2008;132:487–98.
24. Baumann M, Krause M, Hill R. Exploring the role of cancer stem cells in radioresistance. Nat Rev Cancer 2008;8:545–54.
25. Bao S, Wu Q, McLendon RE, Hao Y, Shi Q, Hjelmeland AB, et al. Glioma stem cells promote radioresistance by preferential activation of the DNA damage response. Nature 2006;444:756–60.
26. Phillips TM, McBride WH, Pajonk F. The response of CD24(−/low)/CD44 +breast cancer-initiating cells to radiation. J Natl Cancer Inst 2006;98:1777–85.
27. Nakayama KI, Nakayama K. Ubiquitin ligases: cell-cycle control and cancer. Nat Rev Cancer 2006;6:369–81.
28. Lee J, Kotliarova S, Kotliarov Y, Li A, Su Q, Donin NM, et al. Tumor stem cells derived from glioblastomas cultured in bFGF and EGF more closely mirror the phenotype and genotype of primary tumors than do serum-cultured cell lines. Cancer Cell 2006;9:391–403.
29. Ricci-Vitiani L, Lombardi DG, Pilozzi E, Biffoni M, Todaro M, Peschle C, et al. Identification and expansion of human colon-cancer-initiating cells. Nature 2007;445:111–5.
30. Fujiwara T, Kagawa S, Kishimoto H, Endo Y, Hioki M, Ikeda Y, et al. Enhanced antitumor efficacy of telomerase-selective oncolytic adenoviral agent OBP-401 with docetaxel: preclinical evaluation of chemovirotherapy. *Int J Cancer* 2006;119:432–40.
31. Liu D, Kojima T, Ouchi M, Kuroda S, Watanabe Y, Hashimoto Y, et al. Preclinical evaluation of synergistic effect of telomerase-specific oncolytic virotherapy and gemcitabine for human lung cancer. Mol Cancer Ther 2009;8:980–7.
32. Dean M, Fojo T, Bates S. Tumour stem cells and drug resistance. Nat Rev Cancer 2005;5:275–84.
33. Ma S, Lee TK, Zheng BJ, Chan KW, Guan XY. CD133+ HCC cancer stem cells confer chemoresistance by preferential expression of the Akt/PKB survival pathway. Oncogene 2008;27:1749–58.
34. Cheng T, Rodrigues N, Shen H, Yang Y, Dombkowski D, Sykes M, et al. Hematopoietic stem cell quiescence maintained by p21cip1/waf1. Science 2000;287:1804–8.
35. Liu Y, Elf SE, Miyata Y, Sashida G, Huang G, Di Giandomenico S, et al. p53 regulates hematopoietic stem cell quiescence. Cell Stem Cell 2009;4:37–48.
36. Sutterluty H, Chatelain E, Marti A, Wirbelauer C, Senften M, Muller U, et al. p45SKP2 promotes p27Kip1 degradation and induces S phase in quiescent cells. Nat Cell Biol 1999;1:207–14.
37. Kamura T, Hara T, Matsumoto M, Ishida N, Okumura F, Hatakeyama S, et al. Cytoplasmic ubiquitin ligase KPC regulates proteolysis of p27 (Kip1) at G1 phase. Nat Cell Biol 2004;6:1229–35.
38. Lomazzi M, Moroni MC, Jensen MR, Frittoli E, Helin K. Suppression of the p53- or pRB-mediated G1 checkpoint is required for E2F-induced S-phase entry. Nat Genet 2002;31:190–4.
39. Steegenga WT, van Laar T, Riteco N, Mandarino A, Shvarts A, van der Eb AJ, et al. Adenovirus E1A proteins inhibit activation of transcription by p53. Mol Cell Biol 1996;16:2101–9.

OPEN ACCESS Freely available online

PLOS | ONE

Development of a Clinically-Precise Mouse Model of Rectal Cancer

Hiroyuki Kishimoto[1,2,3], Masashi Momiyama[1], Ryoichi Aki[1], Hiroaki Kimura[1], Atsushi Suetsugu[1], Michael Bouvet[2], Toshiyoshi Fujiwara[3], Robert M. Hoffman[1,2]*

1 AntiCancer, Inc., San Diego, California, United States of America, **2** Department of Surgery, University of California San Diego, San Diego, California, United States of America, **3** Division of Surgical Oncology, Department of Surgery, Okayama University Graduate School of Medicine, Dentistry and Pharmaceutical Sciences, Okayama, Japan

Abstract

Currently-used rodent tumor models, including transgenic tumor models, or subcutaneously growing tumors in mice, do not sufficiently represent clinical cancer. We report here development of methods to obtain a highly clinically-accurate rectal cancer model. This model was established by intrarectal transplantation of mouse rectal cancer cells, stably expressing green fluorescent protein (GFP), followed by disrupting the epithelial cell layer of the rectal mucosa by instilling an acetic acid solution. Early-stage tumor was detected in the rectal mucosa by 6 days after transplantation. The tumor then became invasive into the submucosal tissue. The tumor incidence was 100% and mean volume (±SD) was 1232.4 ± 994.7 mm^3 at 4 weeks after transplantation detected by fluorescence imaging. Spontaneous lymph node metastasis and lung metastasis were also found approximately 4 weeks after transplantation in over 90% of mice. This rectal tumor model precisely mimics the natural history of rectal cancer and can be used to study early tumor development, metastasis, and discovery and evaluation of novel therapeutics for this treatment-resistant disease.

Citation: Kishimoto H, Momiyama M, Aki R, Kimura H, Suetsugu A, et al. (2013) Development of a Clinically-Precise Mouse Model of Rectal Cancer. PLoS ONE 8(11): e79453. doi:10.1371/journal.pone.0079453

Editor: Matthew, Stanford University, United States of America

Received August 27, 2013; **Accepted** October 1, 2013; **Published** November 12, 2013

Funding: This work was supported in part by grants from Young Scientists (B), The Ministry of Education, Culture, Sports, Science and Technology, Japan (H.K.). The funders had no role in study design, data collection and analysis, decision to publish, or preparation of the manuscript.

Competing Interests: The authors have the following interests: Hiroyuki Kishimoto, Masashi Momiyama, Ryoichi Aki, Hiroaki Kimura, Atsushi Suetsugu were former affiliates of AntiCancer Inc. Robert M. Hoffman is a non-salaried affiliate of AntiCancer Inc. AntiCancer Inc. markets animal models of cancer. There are no other competing interests. There are no patents, products in development or marketed products to declare. This does not alter the authors' adherence to all the PLOS ONE policies on sharing data and materials, as detailed online in the guide for authors.

* E-mail: all@anticancer.com

Introduction

Heterotopic implantation models such as subcutaneous tumor implants in mice have been traditionally used to evaluate antitumor treatment because of their reproducibility and monitoring of tumor formation. However, heterotopic models do not have corresponding tumor microenvironments (TME) [1].

Genetically-engineered mouse models of cancer usually require a long time to develop tumors and are unpredictable with regard to frequency, time, and location of primary tumors and even more unpredictable when and where metastasis occurs. Since tumor development in these animals is rarely synchronous, a large cohort of animals must be housed in order to prepare for sufficient numbers of animals at appropriate stages of cancer. Large numbers of animals need to be examined over long periods of time to evaluate cancer treatment, and only survival is often used as an endpoint due to the difficulty of monitoring when tumors appear in internal organs [2].

Several kinds of models employing orthotopic implantation of tumors have been developed and utilized to mainly investigate antitumor drug efficacy [3]. In these models, either cancer cell suspensions are injected into the orthotopic organ or tumor tissue fragments are sutured on the corresponding organ [4,5] with implantation of tissue fragments having been shown to be more accurate [5,6]. With regard to colorectal cancer models, tumors have been established in submucosal tissues or on the colonic serosa, but not on the mucosal surface from which tumors actually arise in patients.

The aim of this study was to establish a "true" clinically-precise orthotopic rectal model in which tumors start forming in the mucosal tissue of the rectum.

Materials and Methods

Cell culture

The mouse colorectal cancer cell line CT26 and the human colorectal cancer cell line HCT-116 were cultured in RPMI 1640 medium supplemented with 10% FBS. CT26 is an N-nitroso-N-methylurethane-(NNMU)-induced mouse undifferentiated colon carcinoma cell line [7]. HCT-116 was derived from a primary human colon cancer specimen [8].

GFP and RFP vector production

The pLEIN retroviral vector (Clontech), expressing enhanced green fluorescent protein (GFP) and the neomycin resistance gene on the same bicistronic message, was used as a GFP expression vector. PT67, an NIH3T3-derived packaging cell line, expressing the 10 Al viral envelope, was purchased from Clontech Laboratories, Inc. PT67 cells were cultured in DMEM supplemented with 10% FBS. For GFP vector production, PT67

packaging cells, at 70% confluence, were incubated with a precipitated mixture of DOTAP™ reagent (Boehringer Mannheim, Indianapolis, Indiana), and saturating amounts of pLEIN plasmid for 18 h. Fresh medium was replenished at this time. The cells were examined by fluorescence microscopy 48 h post-transduction. For selection, the cells were cultured in the presence of 500–2,000 μg/ml of G418 (Life Technologies, Grand Island, New York) for 7 d. The isolated packaging cell clone was termed PT67-GFP [9–12].

For RFP retrovirus production, the *Hind*III/*Not*I fragment from pDsRed2 (Clontech), containing the full-length RFP cDNA, was inserted into the *Hind*III/*Not*I site of pLNCX2 (Clontech) containing the neomycin-resistance gene. PT67 cells were cultured in DMEM supplemented with 10% FBS. For vector production, the PT67 packaging cells, at 70% confluence, were incubated with a precipitated mixture of LipofectAMINE reagent (Life Technologies) and saturating amounts of pLNCX2-DsRed2 plasmid for 18 h. Fresh medium was replenished at this time. The cells were examined by fluorescence microscopy 48 h post-transduction. For selection of a clone producing high amounts of RFP retroviral vector (PT67-DsRed2), the cells were cultured in the presence of 200 to 1,000 μg/mL G418 (Life Technologies) for 7 d. The isolated packaging cell clone was termed PT67-DsRed2 [9–12].

GFP and RFP gene transduction of cancer cell lines

For GFP and RFP gene transduction, the cancer cells were incubated with a 1:1 precipitated mixture of retroviral supernatants of PT67-GFP or PT67-DsRed2 cells and RPMI 1640 containing 10% FBS for 72 h. Fresh medium was replenished at this time. Cells were harvested by trypsin/EDTA 72 h post-transduction and subcultured at a ratio of 1:15 into selective medium, which contained 200 μg/ml of G418. The level of G418 was increased up to 800 μg/ml in a stepwise manner. Clones expressing high levels of GFP or RFP were isolated with cloning cylinders (Bel-Art Products) using trypsin/EDTA and amplified by conventional culture methods in the absence of selective agent [9–12].

Mice

Nude *nu/nu* mice (AntiCancer, Inc., San Diego, CA) were kept in a barrier facility at AntiCancer, Inc., under HEPA filtration and fed with autoclaved laboratory rodent diet (Tecklad LM-485, Western Research Products, Orange, CA). All animal studies were conducted with an AntiCancer Institutional Animal Care and Use Committee (IACUC)-protocol specifically approved for this study and in accordance with the principals and procedures outlined in the National Institute of Health Guide for the Care and Use of Animals under Assurance Number A3873-1. All animal procedures were performed under anesthesia using s.c. administration of a ketamine mixture (10 μl ketamine HCL, 7.6 μl xylazine, 2.4 μl acepromazine maleate, and 10 μl PBS).

Nestin-driven green fluorescent protein (ND-GFP) nude mice

Interaction of the CT26-RFP tumor and host ND-GFP-expressing cells in the rectal mucosa was examined. CT26-RFP cells were orthotopically transplanted to ND-GFP nude mice [13] by the methods described below. Ten days after tumor transplantation, mice were sacrificed and the anorectum was dissected. Tumor and ND-GFP cell interaction was observed with the OV100 imaging system.

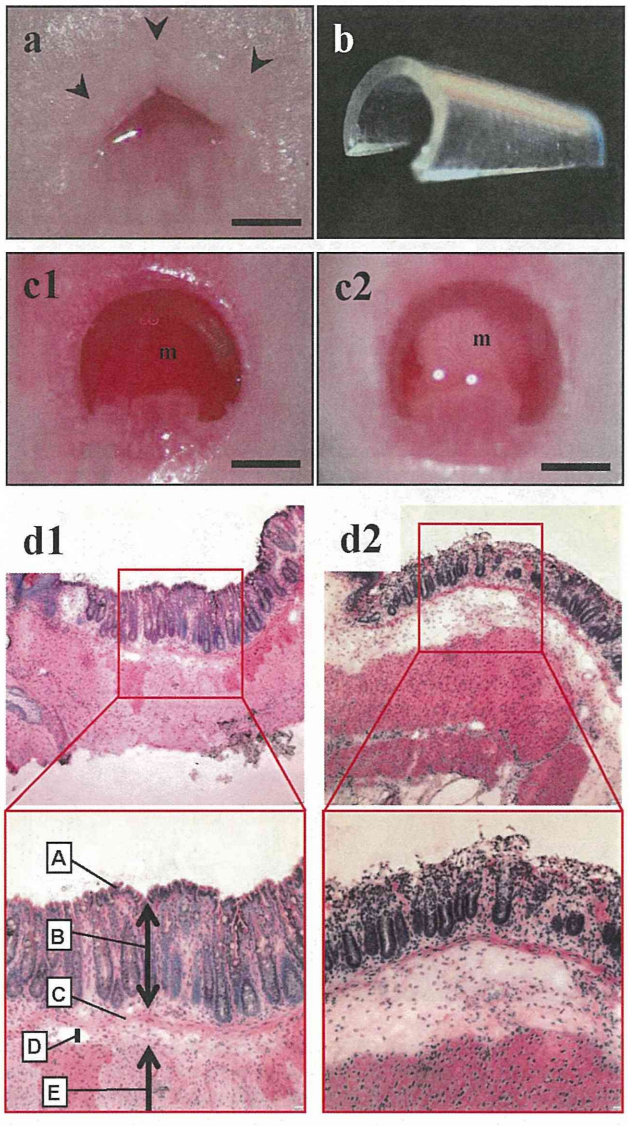

Figure 1. Disruption of the mucosal barrier of the rectum. (**a**) Normal appearance of mouse anus. Scale bar, 1 mm. (**b**) Retractor made from a drip infusion tube. (**c**) The anorectal lumen was dilated by inserting the retractor into the anorectum and instilled with an acetic acid solution. (**c1**) Before acetic acid preparation. (**c2**) The color of the rectal mucosa changed from reddish pink to whitish after treatment with acetic acid solution. m = rectal mucosa. Scale bar, 1 mm. (**d**) Histological examination just after acetic acid treatment showed that the epithelial cell layer of the rectal mucosa was traumatized. (**d1**) H&E section of normal anorectum. A = surface epithelium; B = mucosa; C = muscularis mucosae; D = submucosa; E = muscularis externa. (**d2**) After acetic acid treatment. Note that only the upper part of the mucosa is disrupted. Top, × 40 magnification; bottom, × 100 magnification.
doi:10.1371/journal.pone.0079453.g001

Disruption of the rectal mucosal barrier

The rectal mucosal barrier was chemically disrupted by the following procedure: After mice were anesthetized, a polyethylene catheter was inserted into the rectal lumen through the anus. The rectal lumen was washed with 6 ml PBS to clean out the bowel contents. The rectal lumen was dilated by inserting a retractor into the anorectal region, and then the rectal mucosa was well soaked with 4% acetic acid solution for two minutes, followed by flushing with 6 ml PBS (Fig. 1).

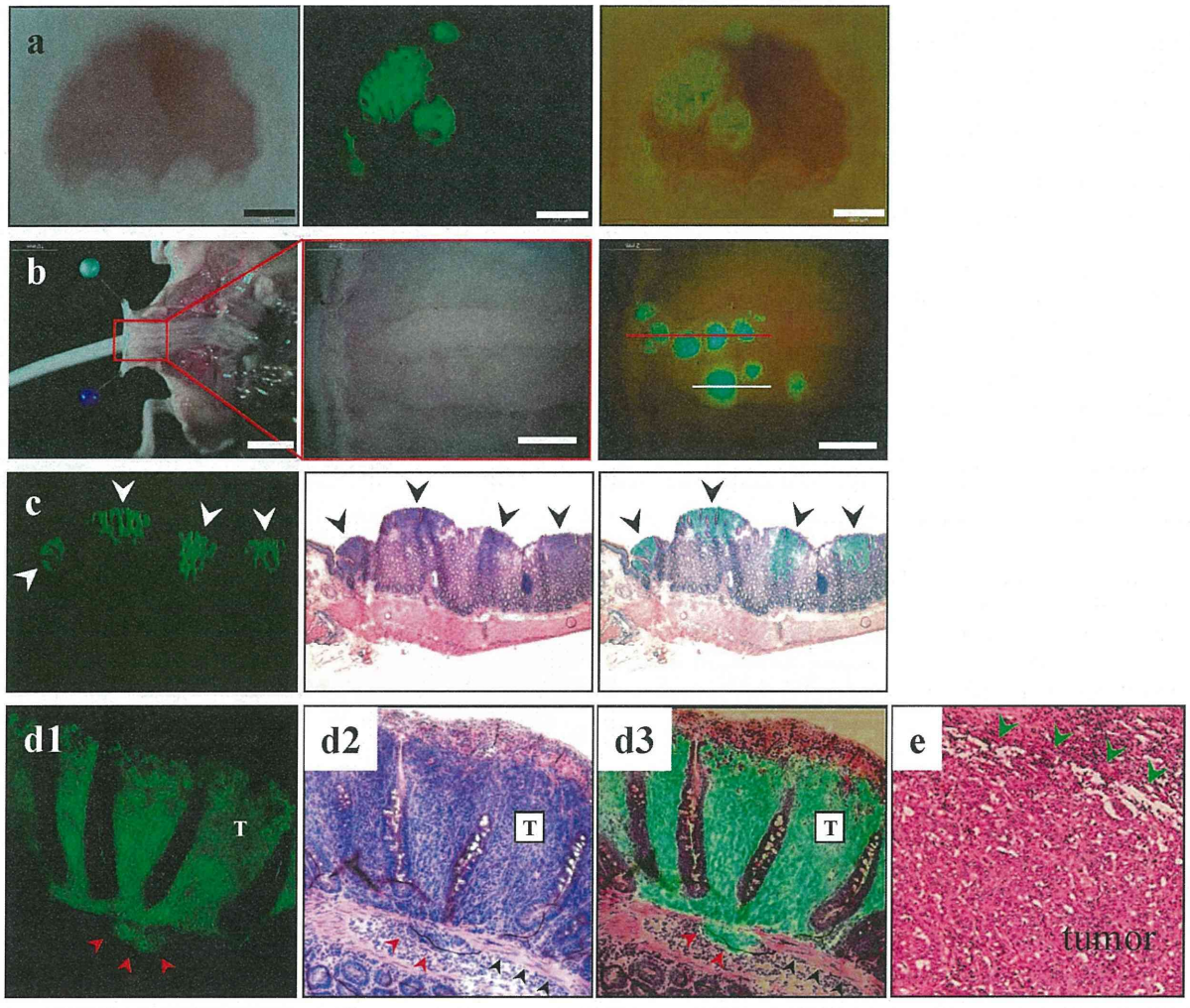

Figure 2. Intramucosal CT26-GFP tumor formation in the mouse rectum. (**a**) The rectum was imaged noninvasively 10 days after implantation. Left, brightfield observation; middle, CT26-GFP tumors growing on the rectal mucosa were clearly visible under fluorescence observation; right, simultaneous observation under bright-light and fluorescence imaging. Scale bar, 500 μm. (**b**) After laparotomy, the rectum was opened longitudinally from the anterior wall. Left, gross appearance of the abdominal cavity. Scale bar: 10 mm; middle, detail of the boxed region; right, simultaneous observation under bright-light and fluorescence. The location of tumor formation was limited on the posterior wall of the terminal rectum. Red line, the direction of rectal cross-section of (**c**). White line, the direction of tumor cross-section of (d). Scale bar, 2 mm. (**c**) Histological analysis confirmed that GFP-positive lesions were medullary-type adenocarcinomas with no glandular structures. Left, fluorescence detection of tumors in a frozen section; middle, GFP-positive tumors showed high cellularity and were confirmed as tumors growing in the mucosal layer of the rectum; right, merged image of H&E histological section and fluorescence detection. Note that cancer cells locate only in the mucosal layer of the rectum. (**d1-3**) CT26 medullary-type adenocarcinomas invading the submucosal layer beyond the limits of the muscularis mucosae (red arrow heads). T = tumor. Black arrow heads, muscularis mucosae. (**e**) Histological appearance of human medullary-type adenocarcinoma. Green arrow heads indicate tumor edge [23].
doi:10.1371/journal.pone.0079453.g002

Intrarectal instillation of colorectal cancer cells and examination for tumor formation

Immediately after disruption of the rectal mucosal barrier, CT26-GFP cells (2.0×10^6) in 50 μl Matrigel (BD Biosciences, San Jose, CA), were introduced and instilled on the rectal mucosal surface with a 28-gage needle inserted 4 mm from the anal ring. The anus was sealed, holding the retractor in the rectum, by plastic tape immediately after instillation of cancer cells to prevent cell leakage. The plastic tape sealing and the retractor in the rectum were removed from the mice after they recovered from anesthesia. After cancer-cell implantation, noninvasive observation with the OV100 Small Animal Imaging System [14] or the MVX-10 fluorescence microscope [15] (both from Olympus, Tokyo, Japan) was used to detect and characterize implanted cancer cells. Then mice were euthanized to explore possible metastasis and for histological studies. The tumor volume was calculated according to the following equation: Tumor volume (mm^3) = length (mm) × width (mm) × depth (mm) × 0.5 [16].

Fluorescence optical imaging and processing

The OV100 Imaging System and MVX-10 fluorescence microscope were used for fluorescence detection of the growing tumor. High-resolution images were directly captured on a PC and analyzed with CellR software (Olympus-Biosystems, Melville, NY) [14].

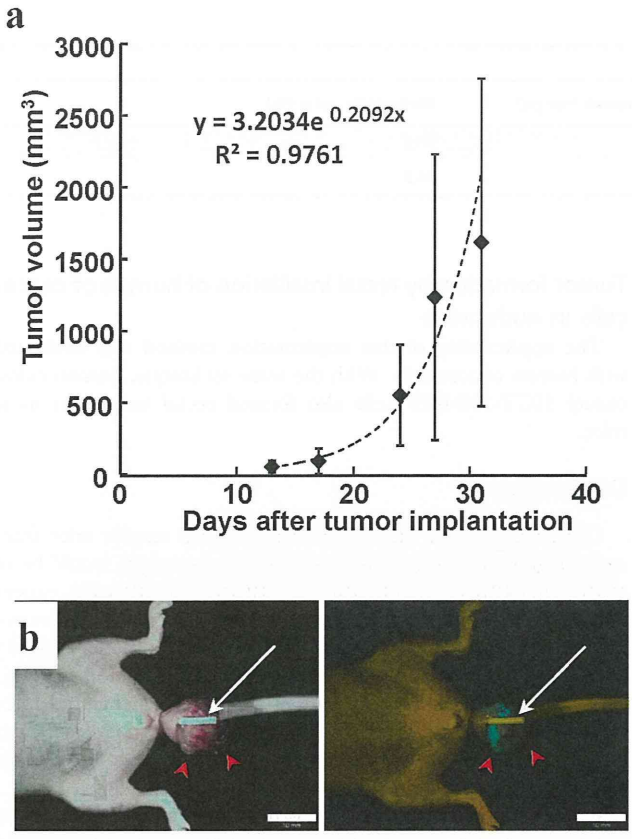

Figure 3. Growth kinetics of CT26-GFP rectal tumors in mice. (**a**) All the mice eventually had only a single tumor formed on the rectal mucosa. Tumor size increased over time. (**b**) Prolapsed CT26 rectal tumor growing outside of the anus at 4 weeks after implantation (red arrow heads). White tube inserted into the rectum (white arrow) shows that anorectal passage is well preserved, and there is no obstruction. Scale bar, 10 mm
doi:10.1371/journal.pone.0079453.g003

Histological Examination

After mice were euthanized, the rectum was opened longitudinally and inspected for the presence of tumors. The excised rectal tumor was then embedded in freezing medium, frozen and sectioned at 7 μm with a cryostat. Slides were observed for tumor cell fluorescence and subsequently examined microscopically by hematoxylin-eosin staining.

Results

Disruption of the mucosal barrier of the rectum

The mucosal barrier of the rectum of nude mice was disrupted by treating the mucosa with 4% acetic acid solution (Fig. 1a-c). There were no deaths or overt toxicity related to this procedure. Histological examination revealed that the epithelial cell layer of the rectal mucosa was disrupted and peeled after acetic acid treatment (Fig. 1d). The mucosal tissue was now ready to accept the cancer cells.

Orthotopic implantation of CT26-GFP cells

Immediately after chemical disruption of the rectal mucosal barrier, CT26-GFP mouse colorectal cancer cells, mixed in Matrigel, were introduced into the rectal lumen. The anus was sealed with plastic tape after filling the rectal lumen with the cancer-cell suspension, which ensured that the cancer cells remained on the rectal mucosa during anesthesia. The total procedure time was approximately 15 min per mouse, and there were no complications or deaths related to both acetic acid treatment and cancer-cell implantation.

After cancer-cell implantation, the rectal lumen was noninvasively examined with the MVX-10 fluorescence microscope or OV100 Small Animal Imaging System (Fig. 2a). The CT26-GFP cells on the rectal mucosa could be readily imaged by GFP fluorescence beginning 6 days after implantation at the latest. The incidence of rectal tumors in the rectal mucosa was 100%. Neither instillation of cancer cells alone or acetic acid treatment alone resulted in growth of a rectal tumor.

As shown in Fig. 2b, the location of tumor formation was limited to the posterior wall of the terminal rectum. This limitation of tumor formation might be due to allowing the cancer-cell

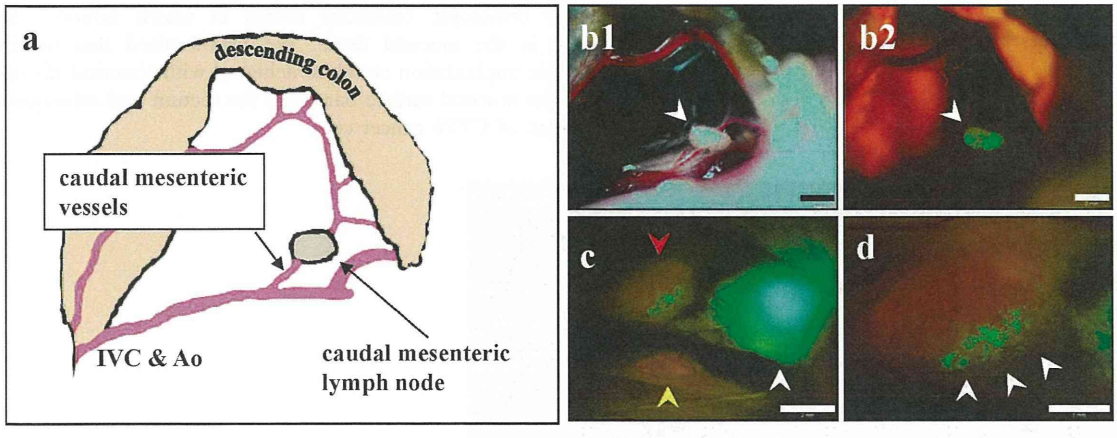

Figure 4. Spontaneous lymph nodes metastasis. (**a**) Schematic drawing of the anatomy in (**b**). The caudal mesenteric lymph node at the origin of the caudal mesenteric artery. This lymph node is equivalent to the inferior mesenteric lymph node in humans. Scale bar, 2 mm. (**b1**) Caudal mesenteric lymph node under bright-light observation. (**b2**) GFP fluorescence of the caudal mesenteric lymph node in (**b1**), indicating that the lymph node contained a metastasis. Scale bar, 2 mm. (**c**) Two para-aortic lymph nodes (red and yellow arrows) were identified in another mouse. White arrow indicates metastasized caudal mesenteric lymph node. Scale bar, 2 mm. (**d**) Higher magnification observation of a para-aortic lymph node indicated by red arrow in (**c**). GFP fluorescence of a micro-metastasis was detected (white arrows). Scale bar, 1 mm.
doi:10.1371/journal.pone.0079453.g004

Table 1. Lymph node metastasis of the rectal tumor.

Lymph node (LN)	Number of metastatic LN/mouse (range)	Metastatic rate (%)
Caudal mesenteric LN	0–1	90.9
Para-Aortic LN	0–2	54.5

doi:10.1371/journal.pone.0079453.t001

suspension to contact only the disrupted dorsal mucosa of the rectum.

At 10 days after implantation, fluorescence microscopy of frozen sections and histological analyses revealed that tumors were growing in the mucosal layer in a similar fashion to human medullary colon carcinoma (Fig. 2c-e). Around this time, CT26-GFP cells invading the submucosal layer, beyond the limits of the muscularis mucosae, were also detected (Fig. 2d).

All the mice eventually had only a single tumor formed on the rectal mucosa, and the tumor size gradually increased over time (Fig. 3a). Since the rectal tumors prolapsed through the anus when they reached approximately 3 mm in size and then grew outside of the anus, no rectal obstruction occurred during the whole observation period in any of the mice (Fig. 3b).

At 4 weeks after instillation of cancer cells, the mean tumor volume (mean volume ± SD) reached 1232.4 ± 994.7 mm^3 (Fig. 3a), and spontaneous lymph node metastases were detected with high occurrence (Fig. 4). The metastatic rate to the caudal mesenteric lymph node (inferior mesenteric lymph node in humans) [17,18], which is a regional lymph node in rectal cancer, was 90.9%. Metastasis to the para-aortic lymph nodes was 54.5% (Table 1). Spontaneous lung metastasis was also detected in 91.8% of mice (Fig. 5). However, only 9% of the mice (1/11) had liver metastasis (Table 2).

At approximately 4 weeks, mice showed cachectic symptoms and had to be sacrificed because of tumor size.

Angiogenesis of mouse rectal tumor orthotopically implanted in ND-GFP nude mice

RFP-expressing CT26 cells were orthotopically implanted into the rectum of nestin-driven GFP (ND-GFP) nude mice by the methods described above. Ten days after implantation, ND-GFP–expressing nascent blood vessels were visualized growing into the RFP-expressing CT26 rectal tumor in the ND-GFP nude mouse (Fig. 6).

Tumor formation by rectal instillation of human of cancer cells in nude mice

The applicability of this implantation method was evaluated with human cancer cells. With the same technique, human colon cancer HCT-116-RFP cells also formed rectal tumors in nude mice.

Discussion

Clinically-accurate animal models in which tumors arise from early-stage and later become invasive and metastatic would be of great value in order to predict clinical outcomes for cancer treatment more precisely. Few transgenic models of invasive colorectal cancer exist [4]. The $Apc^{Min+/-}$ mouse model typically develop adenomas but not invasive adenocarcinomas [19]. Additionally, tumor development in genetically-engineered mice is rarely synchronous, which makes it difficult to prepare sufficient numbers of animals at appropriate stages for cancer treatment evaluation [2].

It has been demonstrated that orthotropic implantation allows the growth and metastatic potential of the transplanted tumors to be expressed and reflect clinical cancer [5,20]. Many colorectal cancer models employing orthotropic implantation have been also reported. However, in these models, either a cancer cell suspension was injected into the submucosal layer of the colorectum [4,5,21], or tumor tissue fragments were simply sutured on the colon serosa. In these models, tumors grow in the submucosal tissues leaving the mucosa (which is the true origin of colorectal cancer) intact or from the beginning tumors grow only on the serosal surface, which is equivalent to advanced stage colorectal cancer in the clinic.

The aim of the present study was to establish a clinically-accurate orthotopic colorectal model in which tumors start forming in the mucosal tissue. We hypothesized that precise orthotopic implantation could be achieved with chemical disruption of the mucosal surface barrier of the rectum and subsequent installation of CT26 cancer cells.

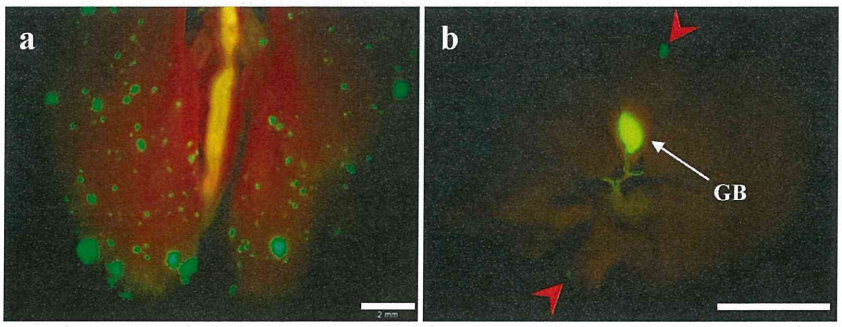

Figure 5. Spontaneous hematogenous metastasis. (**a**) Macroscopic appearance of lung. Lung metastatic foci were detected with GFP fluorescence. Scale bar, 2 mm. (**b**) Macroscopic appearance of the liver. Fluorescence imaging detected GFP expression of CT26-GFP liver metastases (red arrows). Scale bar, 10 mm.
doi:10.1371/journal.pone.0079453.g005

Table 2. Hematogenous metastasis of the rectal tumor.

Organ	Number of metastatic tumor foci/mouse (range)	Metastatic rate (%)
Liver	0–2	9.0
Lung	0–219	91.8

doi:10.1371/journal.pone.0079453.t002

Fluorescently-labeled cancer cells [22] enabled highly sensitive, real-time, and noninvasive detection of very early-stage cancer on the rectal mucosa and micro-metastatic foci in the lymph nodes and the lung, which would be otherwise undetectable in live tissue or even histological examination [20].

The location of primary tumor formation was limited to the posterior wall of the terminal rectum, which is the most convenient observation point in the mouse colorectum. The reproducibility of tumor location allowed easier and more focused noninvasive examination over time. The histological appearance of the tumor was very similar to human colon cancer classified as undifferentiated or medullary-type adenocarcinoma [23].

Lymph node metastases and lung metastasis were detected in the mice implanted with the CT26-GFP cells with high incidence, which could be considered as "true" spontaneous metastasis, since in this method it is highly unlikely that cancer cells can be directly introduced to the venous or lymphatic circulation artificially at the time of implantation [4]. Though liver is a most common metastatic site of colorectal cancer, liver metastasis was found in only 9% of mice (1/11) in this model. This may be explained by the fact that in this model, tumors form at the lower part of the rectum, blood from which drains into the systemic venous circulation dominantly over the portal venous circulation [24]. Rectal cancer is more likely than colon cancer to result in lung metastases without liver metastases in the clinic [24].

Unlike the cecal injection model, this model does not require laparotomy, through which unwanted peritoneal dissemination is caused by cancer cells dissociated at the time of the transplantation [4]. The current method is also applicable in immunocompetent hosts with cancer cell lines of mouse origin and would be suitable for tumor immunology studies.

In ND-GFP nude mice, GFP expression is under the control of the of the nestin promoter [13,25] in which host-derived ND-GFP-expressing blood vessels were visualized in the early stage rectal tumors formed from CT26-RFP cells.

To our knowledge, this is the first model that can reliably provide truly orthotopic rectal cancer growing in the mucosal tissues, and later cause spontaneous lymph node and lung metastasis which are readily detectable by GFP fluorescence with high sensitivity. This model could be used for studying early events in tumor growth or assessing intraluminal factors (dietary compounds, bile acid, intestinal microflora, etc.), that may function to enhance or inhibit the growth of colorectal cancer in early stage cancer.

In conclusion, implantation of cancer cells to the mucosal tissue enabled by the techniques described in the present report allowed the tumors to grow in a manner which mimics clinical human

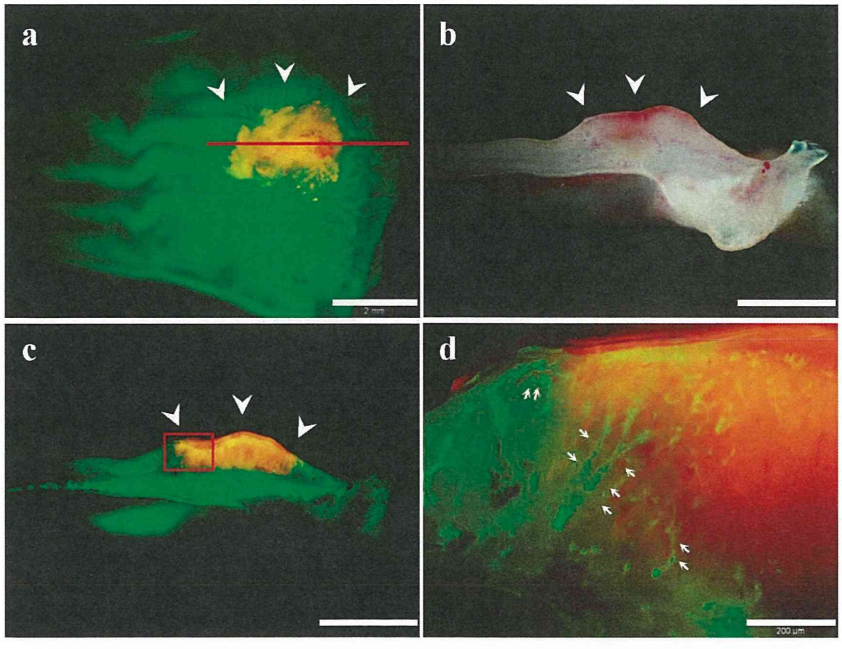

Figure 6. Dual-color imaging of tumor–host interaction in nestin-driven green fluorescent protein (ND-GFP) nude mice. (**a**) CT26-RFP tumor growing in the rectal mucosa of ND-GFP nude mice (white arrow heads). Red line, the direction of the rectal tumor cross-section of (**b**). Scale bar, 2 mm. (**b**) Cross-section of the rectal tumor. Bright- light observation. Scale bar, 2 mm. (**c**) Fluorescence observation of (**b**). Scale bar, 2 mm. (**d**) Detail of the boxed region in (**c**). Host-derived ND-GFP-expressing blood vessels were visualized in the RFP-expressing CT26 rectal tumor in the ND-GFP nude mouse (white arrows). Scale bar, 200 μm.
doi:10.1371/journal.pone.0079453.g006